

Spin pumping in the Heusler alloy $\text{Co}_2\text{FeAl}/\text{MoS}_2$ heterostructure: Ferromagnetic resonance experiment and theory

Sajid Husain,¹ Abhishek Kumar,² Prabhat Kumar,¹ Ankit Kumar,³ Vineet Barwal,¹ Nilamani Behera,³ Sudhanshu Choudhary,² Peter Svedlindh,³ and Sujeet Chaudhary^{1,*}

¹*Thin Film Laboratory, Department of Physics, Indian Institute of Technology Delhi, New Delhi-110016, India*

²*Department of Electronics and Communication Engineering, National Institute of Technology Kurukshetra, Haryana-136119, India*

³*Department of Engineering Sciences, Uppsala University, Box 534, SE-751 21 Uppsala, Sweden*



(Received 21 March 2018; revised manuscript received 21 October 2018; published 14 November 2018)

Spin pumping from the full Heusler alloy Co_2FeAl film into the transition-metal dichalcogenide MoS_2 is reported. Plasma-assisted sulfurization of ion-beam sputtered Mo films of different nominal thicknesses is employed to first fabricate large area high-quality MoS_2 sheets [thicknesses: 1, 2, 3, and 4 monolayers (MLs)] on SiO_2/Si substrates, followed by deposition of Co_2FeAl films with a fixed thickness of 8 nm. The spin pumping is investigated by measuring the changes in the damping constant in the Al(5 nm) capped $\text{Co}_2\text{FeAl}/\text{MoS}_2$ bilayers using ferromagnetic resonance spectroscopy. The study demonstrates that even 1 ML of MoS_2 possesses high enough spin-orbit coupling strength to enhance damping from $5.5(\pm 0.2) \times 10^{-3}$ in Al(5 nm)/ Co_2FeAl (8 nm) to a nearly saturated value of $8.3(\pm 0.2) \times 10^{-3}$ in Al(5 nm)/ Co_2FeAl (8 nm)/ MoS_2 (1 ML), which is suppressed by inserting a thin Al layer at the $\text{Co}_2\text{FeAl}/\text{MoS}_2$ interface. The observed enhancement in damping is in agreement with the results from first-principles calculations based on density functional theory. These results open up a paradigm for designing spintronic devices based on heterostructures comprising a full Heusler alloy and the inherently stable MoS_2 .

DOI: [10.1103/PhysRevB.98.180404](https://doi.org/10.1103/PhysRevB.98.180404)

I. INTRODUCTION

Spintronics offers novel functionalities as well as very promising solutions to the scaling limitations encountered in conventional electronic devices. For example, it is possible to create spin transfer torque (STT) based magnetic random access memories (MRAMs), nano-sized spin-logic devices with suppressed heat dissipation, etc. Recently, in such devices, generation of spin current has been reported for ferromagnetic (FM)/semiconducting bilayer systems [1]. From this perspective, the molybdenum disulfide (MoS_2), which is one of the semiconducting two-dimensional (2D) transition-metal dichalcogenides (TMDs), was theoretically proposed to open up new pathways for spintronic devices [2,3]. Given the possibility to control and limit the number of atomic layers to just one monolayer (ML) and the inherent stability at such small layer thickness, the 2D character of MoS_2 envisions tremendous device potential where interface effects, e.g., spin pumping, are of paramount importance. A ML of MoS_2 consists of a single layer of transition-metal “Mo” atoms sandwiched between two atomic layers of chalcogen “S” atoms in a trigonal prismatic structure. One ML thin MoS_2 does not exhibit the inversion symmetry, and it belongs to the space group $P6m2$ (point group D_{3h}) in which the valence band splits due to the presence of a large spin-orbit coupling (SOC) strength [4]. Thus, compared to other 2D materials such as graphene (which is a weak SOC material [3]), MoS_2 opens up a prospective potential for spintronic applications. Notably, MoS_2 has already been reported for

various other applications such as optoelectronics, solar cells, etc. [5–7]. Importantly, due to the high SOC strength [4], its band structure facilitates the interfacial hybridization. This feature, therefore, generates a variety of promising scenarios where the nonmagnetic (NM) MoS_2 layer is in direct contact with the FM host [8,9]. Furthermore, it will be more advantageous if the FM host is a half-metallic system such as a full Heusler alloy. Among the full Heusler alloys, Co_2FeAl (CFA) has unique characteristics, viz., high Curie temperature (T_C), small Gilbert damping constant (α) [10,11], etc. Recently, it has been evidenced that when grown in direct contact with Ta (a high SOC material), CFA exhibits a fascinating spin texture, i.e., skyrmions [12,13], which are topologically protected chiral spin structures. The small Gilbert damping in CFA makes the alloy interesting for STT-MRAM applications since low α implies a low switching current for the magnetization of the free layer of the magnetic tunnel junction devices [14,15]. In the STT-related applications, conventional NM films, e.g., Pt, Pd, Ta, W, etc., with few nanometer thickness are employed [16–19] owing to their high SOC strength. From this viewpoint, the intrinsically stable 2D dichalcogenides, e.g., MoS_2 , MoSe_2 , MoTe_2 , WS_2 , WSe_2 , WTe_2 , etc., are superior choices for the NM layer in FM/NM bilayer systems, and offer a unique platform for studying the spin-pumping phenomena. The motivation of the present study is to explore the possibility of using 1 ML of MoS_2 in combination with CFA for spin pumping. Compared to the three-dimensional (3D) growth, the 2D growth of MoS_2 is expected to suppress extrinsic contribution to the damping. Being layered materials with monolayer thickness, the influence of SOC at the FM/NM interface can be accurately probed [4].

*Corresponding author: sujeetc@physics.iitd.ac.in

In this Rapid Communication, we have investigated the ferromagnetic resonance (FMR) response in the CFA/MoS₂ bilayers, wherein the thickness of MoS₂ is varied to show the transition from the perfectly interfacial behavior from 1 ML-MoS₂ to 4 ML-MoS₂. The study provides insight into the optimization of the spin current as a result of spin pumping into MoS₂, which is manifested in the form of the enhancement of the damping of the magnetization precession in the CFA layer. The experimental results are compared with the results obtained from density functional theory (DFT) calculations and a very good agreement is observed with regard to spin pumping from CFA to the MoS₂.

II. EXPERIMENTAL DETAILS: METHODS AND MATERIALS

Fabrication of ML-MoS₂. The Mo films of different nominal thicknesses were first deposited on thermally oxidized Si substrates (thickness of SiO₂ \cong 300 nm) at room temperature using an ion-beam sputtering deposition system (NORDIKO-3450). For growing ML-thick MoS₂, the film thickness of Mo was very accurately controlled following the calibration of the deposition rate obtained by performing X-ray reflectivity (XRR) measurements on various Mo films identically sputtered but for different durations. All the samples were prepared at a constant working pressure of $\sim 8 \times 10^{-5}$ Torr (base vacuum $< 1.0 \times 10^{-7}$ Torr), which was dynamically achieved by directly feeding Ar gas at 4 sccm into the two-grid ion source (diam $\sim 4.5''$) operated at a low rf power of 65W. The as-deposited Mo ultrathin films were then transferred to another high vacuum chamber for the sulfurization process [20], which basically involved exposing the Mo films to a H₂S/Ar plasma. In this process, the Mo coated substrates were kept on a Mo boat, which was heated to 450 °C. Afterward, a mixture of H₂S (10%) and Ar (90%) gases was introduced that increased the chamber pressure to 6.5×10^{-1} Torr. A stable and intense plasma was generated by applying a high voltage of 1 kV across two cylindrical-shaped aluminum electrodes facing each other with a spatial separation of 7.5 cm, and the plasma surrounded the Mo boat. The resulting sulfurization process continued for 60 min, after which the plasma, the power to Mo boat, and the supply of H₂S-Ar mixture were shut off simultaneously. The samples were then allowed to cool down in a slightly higher pressure of 9.0×10^{-1} Torr of pure Ar, which was fed to the chamber from a different inlet source.

Growth of Co₂FeAl on MoS₂. After growing MoS₂, the samples were transferred back to the ion-beam sputtering chamber to grow CFA thin films. Then, CFA thin films with fixed thickness (8 nm) were deposited on top of MoS₂ at room temperature, which was followed by annealing the bilayers at 300 °C for 1 h for obtaining the B₂-type ordering in the CFA film. More details related to the growth of B₂-ordered CFA thin films can be found in our previous reports [10–13,21]. Subsequently, all the CFA/MoS₂ bilayers were coated with a 5-nm thin Al cap to protect the CFA from surface oxidation. The layered Al(5)/CFA(8)/MoS₂(1, 2, 3, 4 MLs)/SiO₂/Si heterostructures so formed were used for subsequent characterization.

In addition to the above, some additional samples were also fabricated. These included Al(5)/CFA(8)/SiO₂/Si (i.e., CFA without MoS₂) and Al(5)/CFA(8)/Al(6)/MoS₂(2 ML)/SiO₂/Si samples (i.e., a 6-nm thin Al layer is inserted at the CFA/MoS₂ interface for deliberately preventing the spin pumping into MoS₂). Further, in order to estimate the intrinsic Gilbert damping of CFA and the enhancement in damping due to the spin pumping, the following three different series were also prepared: (a) Al(5 nm)/CFA(6, 8, 10, 12, 15 nm)/Al(6 nm)/SiO₂/Si, (b) Al(5 nm)/CFA(6, 8, 10, 12, 15 nm)/Cu(6 nm)/SiO₂/Si, and (c) Al(5 nm)/CFA(6, 8, 10, 12, 15 nm)/MoS₂(2 ML)/SiO₂/Si.

Basic sample characterization techniques and methods employed for first-principles calculations [22,23] are explained in Sec. S1 of the Supplemental Material [24].

III. RESULTS AND DISCUSSION

A. Structural/thickness analysis of CFA and MoS₂

Figure 1 shows the x-ray diffraction (XRD) pattern of the Al(5 nm)/CFA(8 nm)/MoS₂(3 ML)/SiO₂/Si heterostructure. The occurrence of the (200) diffraction peak is a clear sign of a B₂ ordered CFA layer grown on plasma-assisted MoS₂(3 ML). As inferred from the graph, one can clearly see the presence of the (220) and (400) diffraction peaks, which is indicative of the polycrystalline nature of the CFA thin films. The B₂ ordering parameter can be obtained by using the Webster model [25],

$$S_{B2} = \sqrt{\frac{I_{200}/I_{220}}{I_{200}^{\text{full-order}}/I_{220}^{\text{full-order}}}} \times 100\%, \quad (1)$$

where I_{200}/I_{220} and $I_{200}^{\text{full-order}}/I_{220}^{\text{full-order}}$ represent the experimentally recorded and theoretically calculated intensity ratios for the B₂ ordered structure, respectively. Here, the theoretical intensity ratio has been taken from the ‘‘International diffraction tables for crystallography,’’ Volume C (pp. 555–557) [26]. The estimated value of the ordering parameter S_{B2} is found to be $86.0 \pm 13.6\%$, which is close to the previously reported

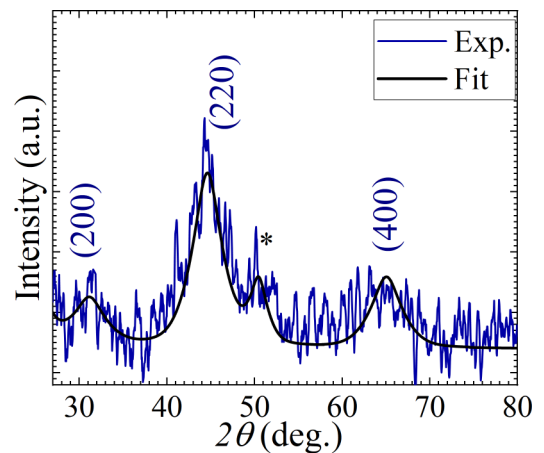


FIG. 1. XRD pattern of Al(5 nm)/CFA(8 nm)/MoS₂(3 ML)/SiO₂/Si sample. Blue and black lines correspond to the experimental and simulated patterns, respectively. Symbol ‘‘*’’ represents a peak corresponding to the substrate.

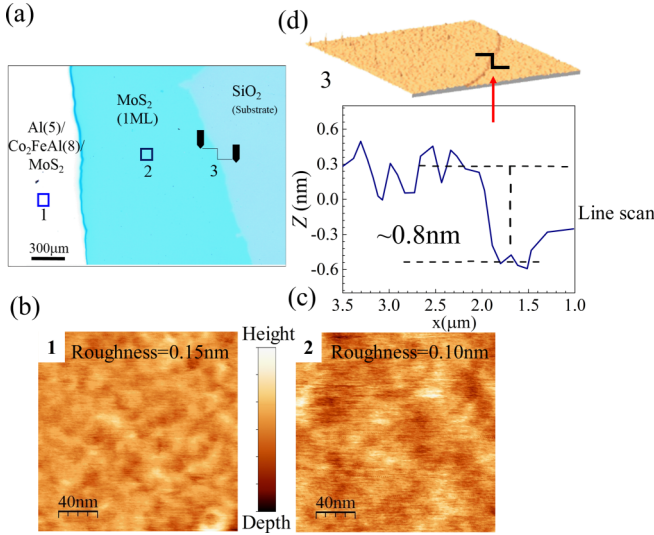


FIG. 2. (a) Optical micrograph showing the top view of the different surface regions (in different colors) of Al(5)/CFA(8)/MoS₂, 1 ML MoS₂, and bare oxidized Si(100) substrate. (b) and (c) are AFM images of regions marked as “1” and “2” in Fig. 1(a) corresponding to Al(5)/CFA(8)/1 ML MoS₂ and 1 ML MoS₂, respectively. (d) The line-scan profile recorded on the step marked as “3” in Fig. 1(a) supporting the formation of 1-ML-thick MoS₂.

results [11,12]. It is inferred from these results that the CFA thin films grown on MoS₂ exhibit the *B2* ordered crystalline phase.

Figure 2(a) shows the optical micrograph (magnification 10×) of the sample Al(5)/CFA(8)/MoS₂ (1 ML) heterostructure (the numbers in parentheses indicate layer thicknesses in nanometers and ML is used for monolayer of MoS₂) as imaged by the 3D optical profilometer. The regions marked as “1” and “2” correspond to the Al/CFA/MoS₂ trilayer and the bottom MoS₂ layer, respectively. The region marked “3” highlights the *height step* where the MoS₂ deposited layer ends on the SiO₂/Si substrate. Since in this particular trilayer specimen, MoS₂ is supposed to be a single ML (as expected from nominal thickness estimation), the surface of each layer is expected to be very smooth with minimal roughness \sim atomic dimensions. Figures 2(b) and 2(c) present the topographical atomic force microscopy (AFM) images recorded at the two different regions noted as “1” and “2” in Fig. 2(a). The image analyses indicate that the *rms* roughness on both the Al(5)/CFA(8) and the 1 ML-MoS₂ surface is ≤ 1.5 Å. Such an ultralow roughness indicates the high quality of the 1 ML-MoS₂ layer with atomically flat surface. The line-scan profile [Fig. 2(d)] recorded over the height step [marked “3” in Fig. 2(a)] also suggests that the thickness of MoS₂ is ~ 1 ML. It is thus concluded that the plasma-assisted sulfurization and the ion-beam sputtering growth have successfully resulted in the formation of a highly smooth Al(5)/CFA(8)/MoS₂ (1 ML) heterostructure with ultralow roughness in the different component layers.

B. Raman analysis: Determination of MoS₂ layers thickness

Figure 3 shows the Raman spectra recorded on various MoS₂ thin films. As stated above, 1 ML of MoS₂ belongs

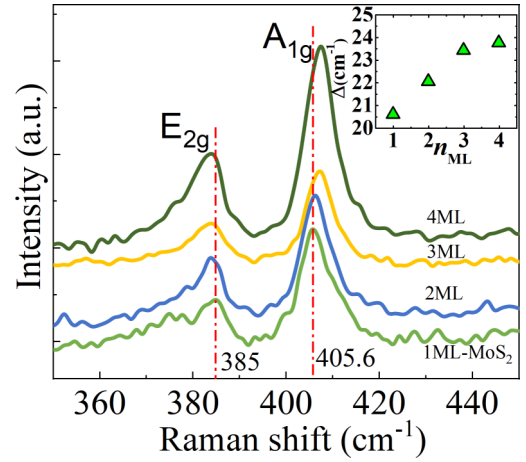


FIG. 3. Raman spectra of MoS₂ films showing the *A*_{1g} and *E*_{2g} modes. The separation between the *A*_{1g} and *E*_{2g} peaks (indicated by the dotted lines) is ~ 20.6 cm⁻¹, which confirms the 1 ML thickness of this particular MoS₂ film. Inset: Observed peak separation (Δ) between the *A*_{1g} and *E*_{2g} modes in the four MoS₂ films having a different number of MLs (*n*_{ML}).

to the *P6m2* space group and comprises a central layer of Mo atoms sandwiched between two layers of S atoms such that there are a total of three atoms in the unit cell [27]. In the MoS₂ lattice structure, the vibrational modes of MoS₂ are represented by 12 irreducible representations, i.e., one mode each of *A*_{1g}, *B*_{1u}, *E*_{1g}, and *E*_{2u}, and two modes each of *A*_{2u}, *B*_{2g}, *E*_{1u}, and *E*_{2g} [28]. Since *E* mode is doubly degenerate, therefore, a total of 18 modes exist in all. Out of these 18 phonon modes, 3 are acoustic, and 15 are optical modes. Among them, *A*_{1g}, *E*_{1g}, *B*_{2g}, and *E*_{2g} are Raman active, and *A*_{2u} and *E*_{1u} are infrared (IR) active [29]. The *A*_{1g} mode corresponds to in-plane symmetric vibrations of the S atoms, and the *E*_{2g} mode corresponds to the out-of-plane asymmetric vibrations of the Mo and S atoms. The *A*_{1g} and *E*_{2g} modes as observed in the Raman spectra recorded on these different MoS₂ films are shown in Fig. 3. One can see that the positions of the *A*_{1g} and *E*_{2g} modes change with the increase in the number of MLs (see inset of Fig. 3). The smallest observed peak separation (Δ) is ~ 20.6 cm⁻¹ in one of the films, which suggests it to be a 1 ML-MoS₂. A similar analysis on other films based on the Δ (shown in the inset of Fig. 3) indicates them to be 2-, 3-, and 4-ML-thick MoS₂ layers consistent with the published result [30].

Having achieved control on the number of MLs in the MoS₂ films, a series of Al(5)/CFA(8)/MoS₂ (1, 2, 3, and 4 ML) heterostructures were fabricated for spin dynamics investigations, which is discussed in detail in the forthcoming section.

C. Magnetization dynamics: FMR measurements

Figure 4(a) shows the FMR spectra recorded on the Al(5)/CFA(8)/1 ML-MoS₂ heterostructure at various frequencies. To estimate the line shape parameters, i.e., resonant field (*H*_r) and linewidth (ΔH), the FMR spectra were fitted with the derivative of a sum of symmetric and antisymmetric Lorentzian functions [10]. Figure 4(b) shows $\mu_0 \Delta H$ vs

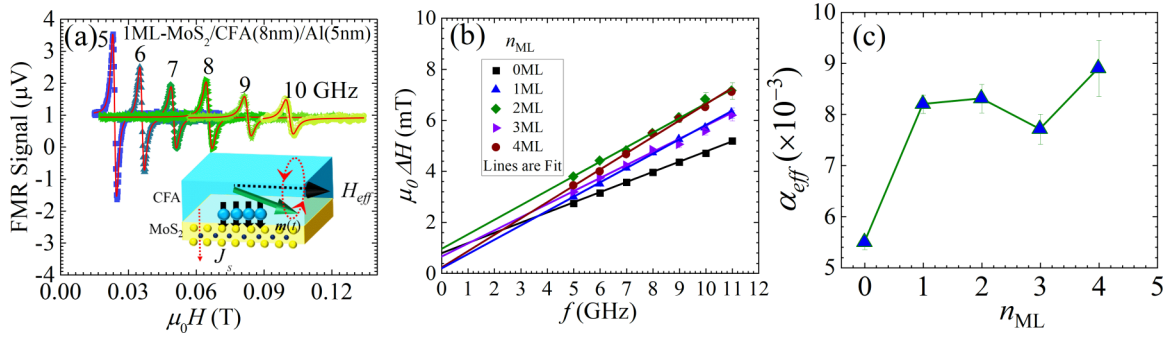


FIG. 4. (a) FMR resonance spectra recorded on an Al(5)/CFA(8)/MoS₂(1 ML) sample by scanning the dc field at various indicated frequencies (Inset: Schematic of the generation and flow of spin current density J_S at CFA/MoS₂ interface as a consequence of transfer of spin angular momentum). (b) Linewidth vs frequency of Al(5)/CFA(8)/MoS₂(n_{ML}) samples, where n_{ML} indicates the number of MLs. (c) α_{eff} vs n_{ML} in these heterostructures.

frequency, and the fit using the empirical relation

$$\mu_0 \Delta H = \mu_0 \Delta H_0 + \frac{4\pi \alpha_{eff} \hbar}{g \mu_B} f, \quad (2)$$

where ΔH_0 is the frequency-independent contribution from sample inhomogeneity and mosaicity. The second term corresponds to a frequency-dependent contribution to the relaxation of the magnetization originating from the intrinsic Gilbert relaxation and the spin-pumping mechanism, etc. Here, g is Lande's splitting factor and is taken to be 2.08 [21], μ_B is the Bohr magneton, \hbar is the reduced Plank's constant, f is the microwave frequency, and $\alpha_{eff} = \alpha_{CFA} + \alpha_{SP}$ is the effective damping parameter where α_{CFA} is the Gilbert damping constant of single layer CFA and α_{SP} is the damping constant due to the spin pumping contribution.

Figure 4(c) shows the observed changes in the damping parameter with number of MoS₂ monolayers (n_{ML}). It is seen that compared to the value of $5.3(\pm 0.2) \times 10^{-3}$ for Al(5)/CFA(8) grown directly on the SiO₂/Si substrate, the damping parameter increases to $8.3(\pm 0.2) \times 10^{-3}$ in the case of Al(5)/CFA(8) grown on 1 ML-MoS₂. This large enhancement in the effective damping for CFA/1 ML-MoS₂ is attributed to the transfer of spin angular momentum into MoS₂ referred to as spin pumping. The parameters of the spin pumping efficiency, i.e., spin mixing conductance and spin diffusion length are found to be $14.9 \pm 2.0 \text{ nm}^{-2}$ and $0.64 \pm 0.25 \text{ nm}$, respectively (see Sec. S2 of the Supplemental Material [24]). Further, the spin memory loss parameter and the spin transparency are also discussed in detail in Sec. S2 of the Supplemental Material [24]. The significant enhancement observed in the damping clearly highlights the presence of a high interfacial SOC suggesting that MoS₂ could be a potential spin-sink material in just 1-ML-thick MoS₂. In a recent publication, Inoue *et al.* formulated the theory of spin pumping into 2D materials when in contact with a FM, which leads to the enhancement of the linewidth in FMR experiments [31]. As presented in the next section, the first-principles calculations also support the enhancement of damping constant in CFA/MoS₂ bilayers compared to bare CFA. Furthermore, as the n_{ML} increases, the damping constant appears to be relatively less affected. The slight variation/discrepancy in the value of α_{eff} observed at higher n_{ML} could be due to the deviations in the experimental growth

parameters, likely to be linked with the sulfurization process step. It is remarkable to note that the extrinsic effects as inferred from the low values of inhomogeneity/mosaicity linewidth broadening $\mu_0 \Delta H_0 < 1 \text{ mT}$ are very small in these Al/CFA/MoS₂ heterostructures. It is also to be noted that the value of $\mu_0 \Delta H_0$ in the CFA/1 ML-MoS₂ sample is negligible, which is consistent with the atomic surface/interface roughness ($\sim 1.5/1.0 \text{ \AA}$) as evidenced in these heterostructures [cf. Figs. 2(b) and 2(c)].

To confirm the existence of spin pumping in the CFA/MoS₂ bilayer, we prepared three different bilayer series of samples with different seed layer materials (of fixed thickness); MoS₂, Al, and Cu with varying thickness of the CFA(t_{CFA}) layer. All these samples are capped with Al to protect from oxidation (see Methods for details). Figure 5(a) shows the effective damping constant $\alpha_{eff}(t_{CFA})$ of the three series, clearly highlighting the difference in $\alpha_{eff}(t_{CFA})$ as the MoS₂ seed layer is replaced with either Al or Cu. It is to be noted that on changing the CFA thickness, the effective damping constant is remarkably increased [cf. Fig. 5(a)] when MoS₂ is used as a seed layer as compared to the case of Al and/or Cu seed layers. In Fig. 5(b), $\alpha_{eff}(t_{CFA})$ is plotted as a function of $1/t_{CFA}$ to extract the intrinsic Gilbert damping of CFA(α_{CFA}) by using the equation [32]

$$\alpha_{eff} = \alpha_{CFA} + \frac{g \mu_B g_{eff}^{\uparrow\downarrow}}{4\pi M s} \frac{1}{t_{CFA}}, \quad (3)$$

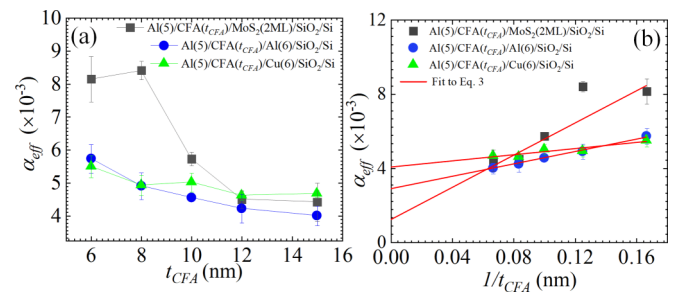


FIG. 5. (a) Effective damping constant (α_{eff}) vs CFA layer thicknesses (t_{CFA}) for various seed layers. Lines are a guide to the eye. (b) α_{eff} vs $1/t_{CFA}$. The intercepts of the fits (solid red lines) using Eq. (3) yield the intrinsic damping α_{CFA} of CFA in the three sample series.

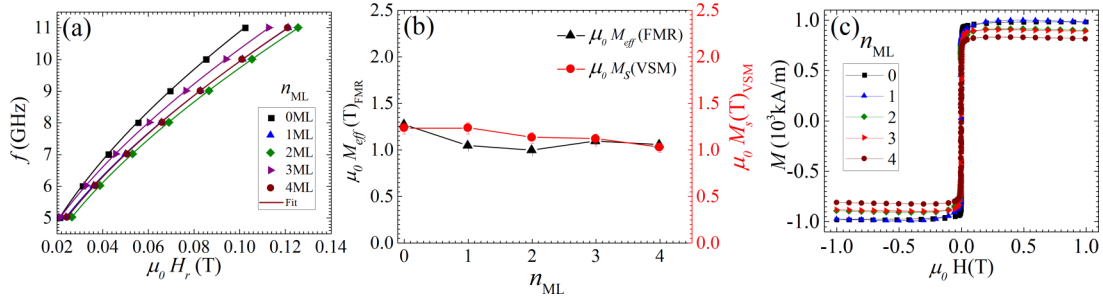


FIG. 6. (a) The resonance field $\mu_0 H_r$ vs f for all Al(5)/CFA(8)/MoS₂(n_{ML}) heterostructures with different n_{ML} [lines are the Kittel's fit to the data using Eq. (2)]. (b) n_{ML} dependence of effective magnetization ($\mu_0 M_{eff}$) and saturation magnetization ($\mu_0 M_S$) obtained from FMR and VSM, respectively. (c) Experimental M - H magnetization loops for all the samples with different n_{ML} .

where the symbols used have their usual meaning. The intercepts of the fits [red lines in Fig. 5(b)] yielded the α_{CFA} values of the three different series of bilayer systems: 0.0012 ± 0.0008 , 0.0028 ± 0.0007 , and 0.0040 ± 0.0002 for Al/CFA(t_{CFA})/MoS₂/SiO₂/Si, Al/CFA(t_{CFA})/Al/SiO₂/Si, and Al/CFA(t_{CFA})/Cu/SiO₂/Si, respectively. The α_{CFA} value obtained for the Si/SiO₂/MoS₂/CFA(t_{CFA})/Al series is consistent with previously reported values [10,11]. The comparatively higher values of α_{CFA} observed in CFA films grown on Cu and Al seed layers suggest that these films possess relatively lower values of S_{B2} compared to the case when CFA is grown on MoS₂. An additional factor could be the islandlike growth of CFA over Cu and/or Al, compared to the 2D growth of CFA expected on the layered MoS₂. These samples having islandlike structures might exhibit more pronounced two-magnon scattering, which is also a reason for higher values of the damping constant in Cu and Al seeded samples. Thus, the intrinsic damping in CFA is different with the different seed layers. The low value of α_{CFA} grown on MoS₂ is consistent with the extremely small rms roughness ~ 1.5 Å observed in CFA(8)/MoS₂(1 ML) [see Fig. 2(c)]. This study further shows that, compared to the intrinsic damping constant α_{CFA} (0.0012 ± 0.0008) of Co₂FeAl, the observed enhancement in damping constant to 0.0083 ± 0.0002 in Al/CFA(t_{CFA})/MoS₂/SiO₂/Si is due to the spin pumping effect across the CFA/MoS₂ interface.

Now, the effective saturation magnetization $\mu_0 M_{eff}$ is determined in the MoS₂ MLs dependent samples using Kittel's equation [10]

$$f(H_r) = \frac{\mu_0 g \mu_B}{2\pi \hbar} [(H_r + H_K)(H_r + H_K + M_{eff})]^{1/2}, \quad (4)$$

where H_K is the anisotropy field and H_r is the resonance field. Figure 6(a) shows the $\mu_0 H_r$ vs f plot. The values of $\mu_0 H_K$ were found to be in the range of 3–5 mT for these samples. Figure 6(b) shows the $\mu_0 M_{eff}$ vs n_{ML} plot. It can be seen that the $\mu_0 M_{eff}$ and $\mu_0 M_S$ values in Al/CFA/MoS₂ are small as compared to the Al capped single CFA layer. This reduction is understandably due to the hybridization effect of Mo and the Co/Fe atoms at the interface [33]. As revealed from the DFT calculations (details in the next section), this hybridization induces a magnetic moment in the adjacent Mo atoms (discussed in the next section) aligned antiparallel to the Co and Fe moments, which reduces the magnetization of CFA. It may also be pointed out here that Cheng *et al.*

proposed that the antiferromagnetic coupling at the interface could also be a source of angular momentum transfer in ferromagnetic/antiferromagnetic bilayer systems [34]. Further, it is found that due to the hybridization effect, the interaction of Co/Fe–Mo d states with the S p states modifies the majority and minority spins which results in a substantial occupancy of the spin up/down states for both Co/Fe, Mo, and S around the Fermi level which is discussed in the next section. Lastly, we do not rule out the finite contributions to the deviations observed in the two values of magnetization that might arise from the presence of finite/weak magnetic anisotropy as reported by Shaw *et al.* [35].

D. Electronic structure and interface effects of CFA/MoS₂ at Fermi level

Figure 7(a) represents the band structure and density of states (DOS) obtained for 1, 2, and 4 MLs of MoS₂ from first-principles calculations. In 1-ML-thick MoS₂, the gap at the K symmetry point provides the direct band transition which is 1.87 eV in our case. Further, in 2 ML MoS₂, the gap reduces to the indirect gap of 1.81 eV shown by the Γ -lowest state in the conduction band. These calculated direct and indirect energy gaps agree with the previous results [36,37]. However, in 4 ML MoS₂, the band gap reduces further to 1.75 eV and gradually saturated to 1.2 eV for pure bulk case (not shown for brevity). From the DOS calculations, the band gap at E_F indicates the semiconducting nature of the MoS₂ for all n_{ML} . Figure 7(b) shows the DOS of CFA (spin-resolved band structure is shown in Sec. S3 of the Supplemental Material [24]). For the majority spin state, the bands can be seen to cross the E_F . In contrast, the minority spin channel exhibits a finite band gap confirming the half-metallicity in this Co₂FeAl full Heusler alloy [11].

In the case of heterostructures consisting of a CFA/MoS₂ interface with different n_{ML} , the calculated DOS are shown in Figure 7(c) for the majority (upper panel) and minority (lower panel) channels. Due to the interfacial hybridization [38] at the CFA/MoS₂ interface, the DOS profiles for the bilayer heterostructures are entirely different in comparison to the isolated CFA and MoS₂. From the calculations for the CFA/MoS₂ system, it is found that the hybridization occurs between the Fe d and S p orbitals and Al p and S p orbitals at the interface and as a result, MoS₂ becomes metallic with large DOS occupancy at E_F . On the other hand,

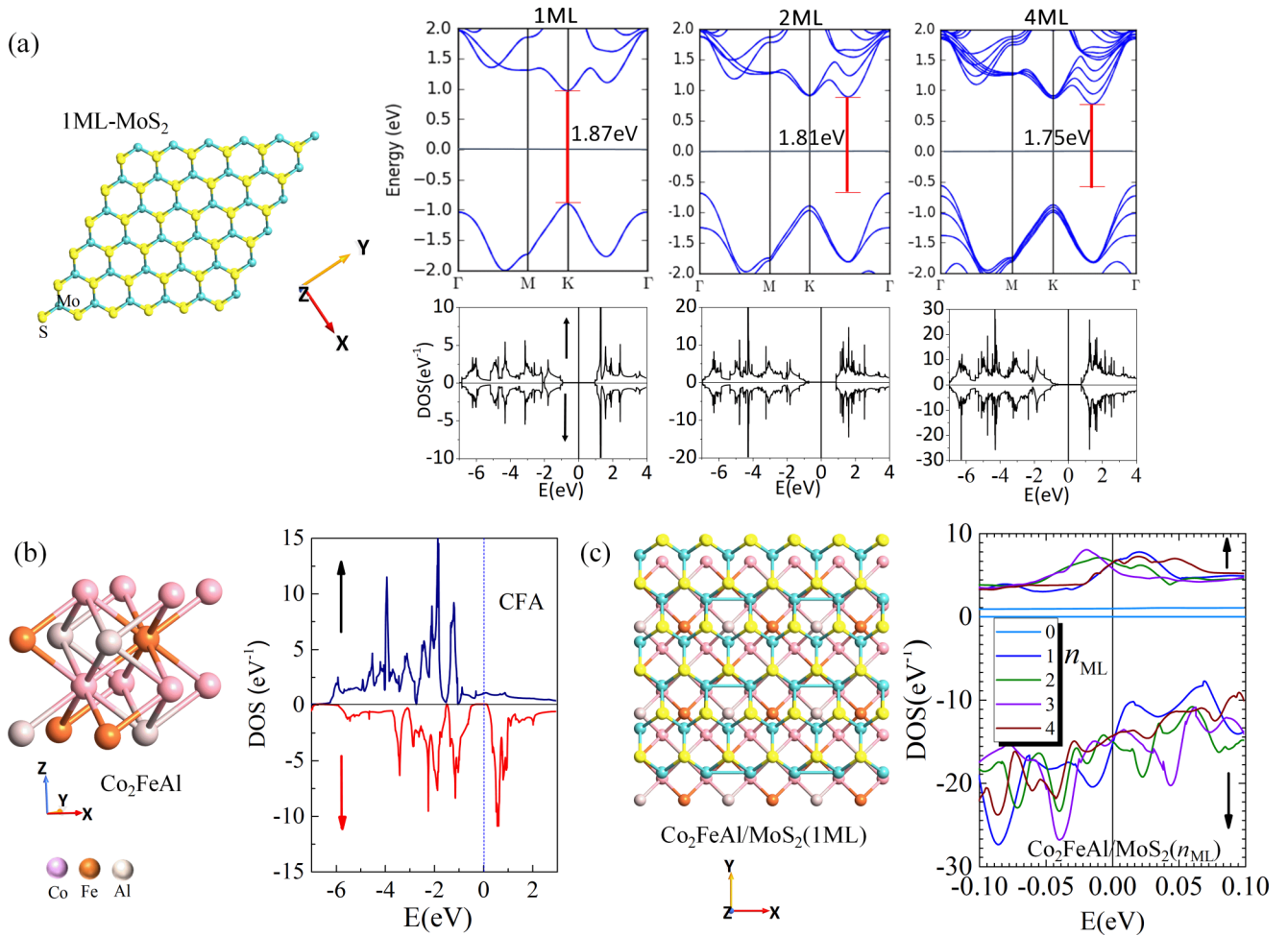


FIG. 7. (a) Energy band structures (top) and DOS plots (bottom) calculated for 1, 2, and 4 MLs of MoS₂, respectively (numbers along with vertical line indicates the band-gap energy). (b) Total DOS for the Co₂FeAl full Heusler alloy. (c) Total DOS resulting from the corresponding interface in the CFA/*n*_{ML}-MoS₂ system (*n*_{ML} : 0–4). The majority and minority states are displayed by up/down arrows. The actual atomic arrangements (geometry and number of atoms) shown to the left of DOS plots in these figures correspond to that used in the DFT calculations in MoS₂, CFA, and the CFA/*n*_{ML}-MoS₂ interface, respectively.

the element-resolved DOS plots at the interface for Fe and Co (see Fig. S5 in the Supplemental Material [24]) revealed the presence of a large DOS at E_F in contrast to the case for bulk CFA. It may also be noted that in CFA/MoS₂ bilayers the DOS at E_F for MoS₂ becomes finite so that MoS₂ at the interface acquires a metal-like character [33,39]. Thus, the presence of large density of states at E_F in MoS₂ at the bilayer interface indicates a strong overlap between wave functions of the CFA and MoS₂ atoms. Further, the change in density of states at the Fermi level affects the spin-relaxation mechanism [40,41]. Kamberský proposed a model wherein the precession of magnetization varies with the changes in the spin DOS at E_F and the spin-orbit energy parameter [40]. Hence, the DOS at E_F provides the information about the magnetization damping in accordance with the relation $G \propto \xi^2 D(E_F)$, where G is the Gilbert relaxation parameter, ξ is the SOC parameter, and $D(E_F)$ is the total spin DOS at E_F . ξ is negligibly small in a single layer of CFA (due to the quenching of orbital moment [42]) and it is constant for MoS₂ (as it exists in the bilayer system in the present study rather than in the form of a single layer). Moreover, ξ is not taken into account

in the calculations of spin-polarized DOS and band structure (since inclusion of SOC then yields eigenstates that are linear combination of up-spin and down-spin states). Hence, qualitatively, G is considered to be proportional to the DOS available at E_F . Experimentally, the G parameter is linked directly with the observed damping/relaxation parameter α_{eff} which can be written as $G = \gamma M_S \alpha_{\text{eff}}$ [41]. Figure 8 shows the n_{ML} dependence of G (left axis) and total DOS (E_F) (right axis) in the CFA/MoS₂ interface in heterostructures calculated from DFT. It is remarkable to note that the n_{ML} dependence of G and DOS(E_F) is qualitatively similar. The low SOC in the single layer CFA film, which results from the quenching of the orbital moment [42], is responsible for the low value of the Gilbert damping constant [$\alpha = 5.5(\pm 0.2) \times 10^{-3}$; cf. Fig. 4(c)]. When CFA is in contact with MoS₂, the large SOC [4] of MoS₂ significantly increases the damping which is a consequence of the large DOS at E_F with the MoS₂ interface. It is to be noted that the DOS does not change much even for higher n_{ML} [cf. Fig. 8(a)], which is also in agreement with the experimentally obtained G parameter. Further, it is important to understand the effect of interfacial coupling on the intrinsic

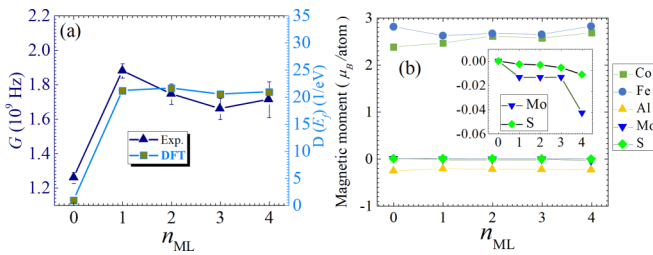


FIG. 8. (a) The n_{ML} dependence of G (left axis) and total DOS(E_F) (right axis) at the CFA/MoS₂ interface in the heterostructures. (b) Theoretically calculated magnetic moments of all the elements effectively contributing to the CFA/MoS₂ interface (Inset: a zoomed view near the origin for highlighting the magnetic moment induced in Mo and S).

moment of Co, Fe, and Al. Figure 8(b) shows the individual magnetic moments of all the atoms present in CFA/MoS₂. The moments induced in the Mo and S are negative (antiparallel to those of Fe and Co). Similar antiferromagnetic contributions from Mo were also predicted previously from DFT calculations in the MoS₂/Fe(Ni) systems [33,38]. The antiparallel alignment of Mo together with the changes in the DOS for the majority and minority bands of Co and Fe atoms in the case of CFA/MoS₂ jointly contribute in the lowering of $\mu_0 M_{\text{eff}}$ and $\mu_0 M_S$ observed in the experimental results [cf. Fig. 6(b)]. Thus with the supporting evidence from the DFT calculations, the experimental observation of large magnetization damping relaxation in CFA in contact with just 1-ML-thick MoS₂ could be of paramount technological significance for next-generation STT and spin-orbit torque based MRAMs, oscillators, and spin-logic devices, etc. However, it is emphasized that further comprehensive theoretical and experimental investigations are required to gain deeper insight about the correlation between the spin-pumping mechanism and

interfacial hybridization induced changes in the density of states in this CFA/MoS₂ system. For this, temperature-dependent FMR measurements on CFA/MoS₂ bilayers, having varying (constant) thickness of CFA (MoS₂), are underway, and the results of which shall be discussed in a separate forthcoming paper.

IV. CONCLUSION

In conclusion, the magnetization-dynamic behavior in the ion-beam sputtered Co₂FeAl(8 nm)/MoS₂(0, 1, 2, 3, 4 MLs) heterostructures has been investigated. Compared to a low Gilbert damping of $5.5(\pm 0.2) \times 10^{-3}$ in a single layer of CFA(8) capped with Al(5), a higher value of $8.3(\pm 0.2) \times 10^{-3}$ is found for the CFA(8)/MoS₂(1–4 MLs) samples, which is attributed to the spin pumping mechanism and damping enhancement which is found to be consistent with the first principle calculations. The damping enhancement in CFA/MoS₂ bilayers obtained with just 1 monolayer of large area high-quality MoS₂ is linked to large SOC-induced interfacial hybridization. These results open up a paradigm for designing spintronic devices based on 1-ML-thick MoS₂ and full Heusler-alloy (CFA) heterostructures, which is indeed indispensable for the number of spintronic applications.

ACKNOWLEDGMENTS

S.H. acknowledges the Department of Science and Technology, Government of India for support through the INSPIRE Fellowship (SR/S9/Z-09/2012). This work was in part supported by Knut and Alice Wallenberg (KAW) Foundation Grant No. KAW 2012.0031. Financial Grants No. 1(1)/2004-M&C, No. 1(14)/2007/M&C, and No. 20(13)/2007-NANO received from Department of Information Technology, Government of India are also acknowledged. The MHRD is also acknowledged for the PPMS facility.

- [1] K. Ando, S. Takahashi, J. Ieda, H. Kurebayashi, T. Trypiniotis, C. H. W. Barnes, S. Maekawa, and E. Saitoh, *Nat. Mater.* **10**, 655 (2011).
- [2] D. Xiao, G.-B. Liu, W. Feng, X. Xu, and W. Yao, *Phys. Rev. Lett.* **108**, 196802 (2012).
- [3] Y. P. Feng, L. Shen, M. Yang, A. Wang, M. Zeng, Q. Wu, S. Chintalapati, and C. R. Chang, *WIREs Comput. Mol. Sci.* **7**, e1313 (2017).
- [4] Z. Y. Zhu, Y. C. Cheng, and U. Schwingenschlögl, *Phys. Rev. B* **84**, 153402 (2011).
- [5] A. Pospischil, M. M. Furchi, and T. Mueller, *Nat. Nanotechnol.* **9**, 257 (2014).
- [6] J.-H. Hur, J. Park, and S. Jeon, *J. Phys. D: Appl. Phys.* **50**, 065105 (2017).
- [7] C.-X. Liu, *Phys. Rev. Lett.* **118**, 087001 (2017).
- [8] Y. Wang, L. Qi, and Y. Wu, *J. Vac. Sci. Technol. A* **35**, 041510 (2017).
- [9] W. Zhang, J. Sklenar, B. Hsu, W. Jiang, M. B. Jungfleisch, J. Xiao, F. Y. Fradin, Y. Liu, J. E. Pearson, J. B. Ketterson, Z. Yang, and A. Hoffmann, *APL Mater.* **4**, 032302 (2016).
- [10] S. Husain, S. Akansel, A. Kumar, P. Svedlindh, and S. Chaudhary, *Sci. Rep.* **6**, 28692 (2016).
- [11] A. Kumar, F. Pan, S. Husain, S. Akansel, R. Brucas, L. Bergqvist, S. Chaudhary, and P. Svedlindh, *Phys. Rev. B* **96**, 224425 (2017).
- [12] S. Husain, A. Kumar, S. Akansel, P. Svedlindh, and S. Chaudhary, *J. Magn. Magn. Mater.* **442**, 288 (2017).
- [13] S. Husain, N. Sisodia, A. K. Chaurasiya, A. Kumar, S. Akansel, A. Barman, P. K. Muduli, P. Svedlindh, and S. Chaudhary, *arXiv:1703.10224*.
- [14] E. Eken, I. Bayram, Y. Zhang, B. Yan, W. Wu, and Y. Chen, *Integr. VLSI J.* **58**, 253 (2017).
- [15] D. Apalkov, A. Khvalkovskiy, S. Watts, V. Nikitin, X. Tang, D. Lottis, K. Moon, X. Luo, E. Chen, A. Ong, A. Driskill-Smith, and M. Krounbi, *ACM J. Emerg. Technol. Comput. Syst.* **9**, 1 (2013).
- [16] Y. Liu, Z. Yuan, R. J. H. Wesselink, A. A. Starikov, and P. J. Kelly, *Phys. Rev. Lett.* **113**, 207202 (2014).
- [17] J.-C. Rojas-Sánchez, N. Reyren, P. Laczkowski, W. Savero, J.-P. Attané, C. Deranlot, M. Jamet, J.-M. George, L. Vila, and H. Jaffres, *Phys. Rev. Lett.* **112**, 106602 (2014).

- [18] A. Kumar, S. Akansel, H. Stopfel, M. Fazlali, J. Åkerman, R. Brucas, and P. Svedlindh, *Phys. Rev. B* **95**, 064406 (2017).
- [19] N. Behera, S. Chaudhary, and D. K. Pandya, *Sci. Rep.* **6**, 19488 (2016).
- [20] P. Kumar, M. Singh, R. K. Sharma, and G. B. Reddy, *Mater. Res. Express* **3**, 055021 (2016).
- [21] S. Husain, A. Kumar, V. Barwal, N. Behera, S. Akansel, P. Svedlindh, and S. Chaudhary, *Phys. Rev. B* **97**, 064420 (2018).
- [22] J. P. Perdew, K. Burke, and M. Ernzerhof, *Phys. Rev. Lett.* **77**, 3865 (1996).
- [23] See <https://quantumwise.com/>.
- [24] See Supplemental Material at <http://link.aps.org/supplemental/10.1103/PhysRevB.98.180404> for experimental methods, theoretical calculation details, spin pumping analysis (spin diffusion length, spin mixing conductance, spin pumping confirmation, and spin memory loss contribution), spin-polarized band structure of CFA, spin DOS for CFA/MoS₂, and CoFe/MoS₂ bilayers (see also Refs. [43–57]).
- [25] P. J. Webster and K. R. A. Ziebeck, *J. Phys. Chem. Solids* **34**, 1647 (1973).
- [26] E. Prince, *International Tables for Crystallography Vol. C* (Wiley-Blackwell, 2004).
- [27] X. Zhang, W. P. Han, J. B. Wu, S. Milana, Y. Lu, Q. Q. Li, A. C. Ferrari, and P. H. Tan, *Phys. Rev. B* **87**, 115413 (2013).
- [28] T. J. Wieting and J. L. Verble, *Phys. Rev. B* **3**, 4286 (1971).
- [29] J. L. Verble and T. J. Wieting, *Phys. Rev. Lett.* **25**, 362 (1970).
- [30] Q. Shao, G. Yu, Y. W. Lan, Y. Shi, M. Y. Li, C. Zheng, X. Zhu, L. J. Li, P. K. Amiri, and K. L. Wang, *Nano Lett.* **16**, 7514 (2016).
- [31] T. Inoue, G. E. W. Bauer, and K. Nomura, *Phys. Rev. B* **94**, 205428 (2016).
- [32] J. M. Shaw, H. T. Nembach, and T. J. Silva, *Phys. Rev. B* **85**, 054412 (2012).
- [33] C. Song, S. Gong, Z. Zhang, H. Mao, Q. Zhao, J. Wang, and H. Xing, *J. Phys. D: Appl. Phys.* **48**, 485001 (2015).
- [34] R. Cheng, J. Xiao, Q. Niu, and A. Brataas, *Phys. Rev. Lett.* **113**, 057601 (2014).
- [35] J. M. Shaw, E. K. Delczeg-Czirjak, E. R. J. Edwards, Y. Kvashnin, D. Thonig, M. A. W. Schoen, M. Pufall, M. L. Schneider, T. J. Silva, O. Karis, K. P. Rice, O. Eriksson, and H. T. Nembach, *Phys. Rev. B* **97**, 094420 (2018).
- [36] K. F. Mak, C. Lee, J. Hone, J. Shan, and T. F. Heinz, *Phys. Rev. Lett.* **105**, 136805 (2010).
- [37] S. W. Han, H. Kwon, S. K. Kim, S. Ryu, W. S. Yun, D. H. Kim, J. H. Hwang, J. S. Kang, J. Baik, H. J. Shin, and S. C. Hong, *Phys. Rev. B* **84**, 045409 (2011).
- [38] K. A. Min, J. Cha, K. Cho, and S. Hong, *2D Mater.* **4**, 024006 (2017).
- [39] K. Dolui, A. Narayan, I. Rungger, and S. Sanvito, *Phys. Rev. B* **90**, 041401(R) (2014).
- [40] V. Kamberský, *Can. J. Phys.* **48**, 2906 (1970).
- [41] S. He, Y. Liu, Y. Zheng, Q. Qin, Z. Wen, Q. Wu, Y. Yang, Y. Wang, Y. Feng, K. L. Teo, and C. Panagopoulos, *Phys. Rev. Mater.* **1**, 064401 (2017).
- [42] S. Trudel, O. Gaier, J. Hamrle, and B. Hillebrands, *J. Phys. D: Appl. Phys.* **43**, 193001 (2010).
- [43] S. Azzawi, A. Ganguly, M. Tokaç, R. M. Rowan-Robinson, J. Sinha, A. T. Hindmarch, A. Barman, and D. Atkinson, *Phys. Rev. B* **93**, 054402 (2016).
- [44] M. Haertinger, C. H. Back, J. Lotze, M. Weiler, S. Geprägs, H. Huebl, S. T. B. Goennenwein, and G. Woltersdorf, *Phys. Rev. B* **92**, 054437 (2015).
- [45] M. Caminale, A. Ghosh, S. Auffret, U. Ebels, K. Ollefs, F. Wilhelm, A. Rogalev, and W. E. Bailey, *Phys. Rev. B* **94**, 014414 (2016).
- [46] W. Zhang, W. Han, X. Jiang, S.-H. Yang, and S. S. P. Parkin, *Nat. Phys.* **11**, 496 (2015).
- [47] C. F. Pai, Y. Ou, L. H. Vilela-Leão, D. C. Ralph, and R. A. Buhrman, *Phys. Rev. B* **92**, 064426 (2015).
- [48] J. Bass and W. P. Pratt, *J. Phys.: Condens. Matter* **19**, 183201 (2007).
- [49] C. T. Boone, J. M. Shaw, H. T. Nembach, and T. J. Silva, *J. Appl. Phys.* **117**, 223910 (2015).
- [50] A. Conca, S. Keller, L. Mihalceanu, T. Kehagias, G. P. Dimitrakopoulos, B. Hillebrands, and E. Th. Papaioannou, *Phys. Rev. B* **93**, 134405 (2016).
- [51] Y. Tserkovnyak, A. Brataas, G. E. W. Bauer, and B. I. Halperin, *Rev. Mod. Phys.* **77**, 1375 (2005).
- [52] A. Allain, J. Kang, K. Banerjee, and A. Kis, *Nat. Mater.* **14**, 1195 (2015).
- [53] Y. J. Zhang, W. Shi, J. T. Ye, R. Suzuki, and Y. Iwasa, *Phys. Rev. B* **95**, 205302 (2017).
- [54] K. Eid, D. Portner, J. A. Borchers, R. Loloee, M. A.-H. Darwish, M. Tsoi, R. D. Slater, K. V. O'Donovan, H. Kurt, W. P. Pratt, Jr., and J. Bass, *Phys. Rev. B* **65**, 054424 (2002).
- [55] A. Sharma, J. A. Romero, N. Theodoropoulou, R. Loloee, W. P. Pratt, and J. Bass, *J. Appl. Phys.* **102**, 113916 (2007).
- [56] H. Kurt, R. Loloee, K. Eid, W. P. Pratt, and J. Bass, *Appl. Phys. Lett.* **81**, 4787 (2003).
- [57] H. Y. T. Nguyen, W. P. Pratt, and J. Bass, *J. Magn. Magn. Mater.* **361**, 30 (2014).